Orexin population activity precisely reflects net body movement across behavioral and metabolic states

Author List: Alexander L. Tesmer[1], Paulius Viskaitis[1], Dane Donegan[1], Eva F. Bracey[1], Nikola Grujic[1], Tommaso Patriarchi[2,3], Daria Peleg-Raibstein[1,3], Denis Burdakov[1,3]

Affiliations:
1: *Swiss Federal Institute of Technology (ETH Zürich), Department of Health Sciences and Technology, Zürich, Switzerland*
2: *Institute of Pharmacology and Toxicology, University of Zürich, Zürich, Switzerland*
3: *Neuroscience Center Zürich (ZNZ), Zürich, Switzerland*

Correspondence: alexander.tesmer@hest.ethz.ch, denis.burdakov@hest.ethz.ch

Abstract:

Tracking net body movement in real time may enable the brain to estimate ongoing demands and thus better orchestrate muscle tone, energy balance, and arousal. To identify neural populations specializing in tracking net body movement, here we compared self-initiated movement-related activity across genetically-defined subcortical neurons in the mouse brain, including dopaminergic, glutamatergic, noradrenergic, and key peptidergic neurons. We show that hypothalamic orexin/hypocretin-producing neurons (HONs) are exceptionally precise movement-trackers, encoding net body movement across multiple classified behaviors with a high degree of precision, independent of head acceleration. This tracking was so precise, that video analysis of the mouse body movement reliably served as a low-cost biometric for HON population activity. The movement tracking was independent of internal nutritional states, and occurred in a communication bandwidth distinct from HON encoding of blood glucose. At key projection targets, orexin/hypocretin peptide outputs correlated with self-initiated movement in a projection-specific manner, indicating functional heterogeneity in HON outputs. Finally, we found that body movement was not encoded to the same extent in other key neural populations related to arousal or energy. These findings indicate that subcortical orchestrators of arousal and metabolism are finely tuned to encode net body movement, constituting a bridge multiplexing ongoing motor activity with internal energy resources.

Introduction

Neural activity related to body movement recently received renewed attention enabled by modern video tracking techniques [1-4]. Although the cortex is classically subdivided into sensory and motor regions[5], movement-related signals make up a large proportion of single-neuron activity across both regions [1-4, 6-18]. Modern technologies for recording large numbers of neurochemically-undefined neurons also detected movement-related activity across subcortical brain areas[1], but suggested some differences between brain areas[3]. This raises the question of whether population activities of neurochemically-distinct subcortical neurons are shaped by the magnitude and frequency of body movements.

We explored this question by examining the population activity of hypothalamic neurons producing the peptide transmitters hypocretins/orexins [19, 20]. Hypocretin/orexin neurons (HONs) track the body's glycemic dynamics and hunger states [20-23], and orchestrate arousal [24-27]. Metrics and interpretations of HON activity are of substantial interest in both basic and clinical sciences, due to their brain-wide influence and link to diagnosis and treatment of multiple brain disorders[28-36]. Yet, fundamental questions remain unresolved in relation to HONs and movement:

- Does HON population activity track specific behaviors, or the general magnitude of body movement?
- Given that hunger attenuates some neural operations [37], does it disable HON movement tracking?
- Is movement vs glycemic information tracked by quantitatively distinct bandwidths of HON activity?
- How does HON tracking of body movement compare to other genetically-defined neural subcortical clusters linked to arousal and metabolism?

Here, we address these questions by simultaneously measuring population HON activity and body movement. We report that HONs encode the instantaneous magnitude of body movement; a feature that was observed across and within unique behaviors. HON movement encoding occurs in an activity bandwidth quantitatively distinct from their glucose-tracking bandwidth and is independent of metabolic or glycemic states. We further find that orexin/hypocretin peptide release dynamics related to body movement differ between various projection targets of orexin neurons. These results define a low-cost video biometric of HONs in a widely-used experimental setting, and add to our understanding of movement-related activation of genetically-distinct subcortical neural clusters.

Results

A general movement metric statistically explains rapid HON population dynamics across and within behaviors

To correlate HON dynamics with general body movement, we used a video camera to monitor n = 15 head-fixed mice on a running wheel. Head fixation allowed us to repeatedly record movement from a fixed angle while focusing on factors other than head acceleration, as done in other recent studies[1, 2]. Simultaneously, we recorded HON activity via intrahypothalamic fiber photometry of HON-selective GCaMP6s activity sensor (Figure 1A). Movement artifacts were controlled for via isosbestic excitation. To measure body movement, we derived a 1-dimensional movement metric by calculating the total per-pixel difference between consecutive frames, and then convolving with a decay kernel matched to the known dynamics of the GCaMP6s sensor (Figure 1B; [38]). We then quantified the correlation between recorded HON dynamics, movement, and running speed on the wheel. HON dynamics exhibited a positive correlation to both running-speed ($r = 0.50 \pm 0.03$) and the movement metric ($r = 0.68 \pm 0.04$, Figure 1C-D). The movement metric's correlation was significantly stronger than running ($p < 0.0001$). Notably, we also observed a positive correlation with the movement metric within epochs containing no locomotion on the wheel ($r = 0.54 \pm 0.03$), demonstrating that movement encoding by HON dynamics is not limited to running (Figure 1C,D).

Does HON activity represent discrete behavioral states, or rather, encode movement magnitude generalized over behaviors? Both hypotheses could potentially explain the correlation in Figure 1. To compare our movement metric (Figure 1B) across different behaviors, we trained a deep-learning network (see methods) to classify video recordings into the five most commonly observed behaviors: resting, running, grooming, chewing, and sniffing (Figure 2A). Recorded HON activity was the highest during running, and lowest during resting showing significantly different activity levels across behaviors ($p < 0.0001$, Figure 2B,C). The average HON activity during specific behaviors followed a nearly 1:1 relationship against its average movement metric (Figure 2D). We then asked whether HON activity could be better explained by a classified behavior, or if it simply followed the movement metric regardless of the specific behavior. To test this, we fit three models in which HON activity was predicted by (1) the classified behavior, (2) the movement metric, or (3) the movement metric as an interaction effect with classified behavior (Figure 2E). Using the Akaike information criterion to assess model fit, we found model 1 was vastly inferior to model 3. However, the strength of this improvement was substantially less when comparing model 2 to model 3. These results suggest that HON activity is tracking the magnitude of movement change, not encoding different types of behavior. Finally, we sought to analyze HON dynamics during transitions between behavioral states. We first identified the six most common behavioral transitions (Figure 2F) and aligned them to both the movement metric and HON activity. As expected, the HON activity strongly resembled the magnitude of body movement exhibited along behavioral transitions (Figure 2G,H).

Movement tracking within different frequencies and phases of HON population signal

Recorded HON dynamics varied over multiple timescales, exhibiting sub-second to several-minute oscillations. Due to this observation, we asked if HON encoding of movement was similar across frequency domains of HON activity. Empirical mode decomposition (EMD) adaptively decomposes a signal into a set of intrinsic mode functions (IMFs) which provide a time-frequency representation of the data, and is robust to the non-stationary and non-linear nature of biological signals[39]. Each IMF can be assigned a characteristic frequency which approximates the average oscillation in that signal component. Thus, we were able to "break down" hORX-GCaMP6s photometry into a set of simple IMFs, each capturing a different characteristic frequency of HON dynamics (Figure 3A). When plotting the average power of each HON IMF versus its characteristic frequency, we noted that maximum power generally occurred around 0.1 to 0.01 Hz (Figure 3B). A parallel EMD performed on the body movement metric revealed a maximum power in a similar frequency band (Figure 3C), suggesting that body movement and HONs have similar spectral profiles.

Do movements occur at specific phases within the HON activity rhythms? To examine this, we performed a phase preference analysis which tells us when, on average, a movement event occurs in the cycle of a HON oscillation. By convention, within each HON IMF, we defined the crest ("upstate") to be at π/2 radians and the trough ("downstate") at 3π/2 radians. In turn, we split the movement metric (z-score) above and below zero to define "active" and "quiescent" movement epochs, respectively. We found that active epochs preferred the π/2 HON phase while quiescent epochs preferred the 3π/2 HON phase, especially in the 0.1 to 0.01 Hz frequency domain (Figure 3D). Strongest phase coupling between HONs and movement was also observed in this frequency domain (Figure 3E).

Finally, we sought to confirm whether HON simply tracked, or also shaped, the body movements characterized in Figure 3C. We reasoned that if HONs only tracked the movements, then HON ablation would not substantially alter the power spectrum of the movements; conversely, if HONs shaped the movements, then HON ablation would alter the movements. We selectively ablated HONs using an extensively validated HON-DTR mouse model[23, 40, 41] (Figure 4A,B). Maximum-power IMFs were found in a similar frequency range peaking around 0.1-0.01 Hz in HON-ablated and control mice (Figure 4C), suggesting HONs are not necessary to maintain movement frequency profiles. To further explore this using an alternative analysis, we used a K-Means clustering algorithm to sort self-initiated movements into two broad categorical clusters constituting "small" and "large" movements (Figure 4D). The frequency of "small" and "large" movements was not different across control and HON-ablated mice (Figure 4E). Overall, these results define frequencies and phases of HON activity that track body movement information.

Orexinergic representation of movement at different HON projection targets

Monoaminergic nuclei producing dopamine and noradrenaline, substantia nigra pars compacta (SNc) and locus coeruleus (LC) respectively, have long been studied for their involvement in arousal and movement [42, 43]. Both are densely innervated by HON axons and express orexin receptors [29, 44]. Do HONs transmit movement information equally to these projection targets? To investigate this, we expressed the genetically-encoded orexin peptide biosensor OxLight1[45] into the SNc and LC for simultaneous dual-site recording in the same mouse (Figure 5A-C). We found that the "active" epochs of the movement metric differed in phase preference to OxLight1 signal between the brain regions: SNc orexin recordings showed a phase preference to the "downstate" (3π/2) phase, while LC orexin recordings preferred the "upstate" (π/2) phase, particularly in the 0.1 to 0.01 Hz frequency band (Figure 5D), with the highest phase coupling in the lower frequency bands (Figure 5E). This suggests that orexin release may heterogeneously represent body movement at different HON projection targets. When orexin dynamics were aligned to "small" and "large" movement clusters, we observed rising signals in the LC, but falling signals in the SNc, which was especially apparent in association with "large" clustered movements (Figure 5F). Together, these analyses indicate that orexin peptide release related to movement is non-homogenous across two major HON projection targets.

HON movement tracking across metabolic states

Given the robust correlation of HON activity and movement across the behavioral and frequency spectra, we sought to contrast our findings against another major physiological factor thought to influence HON activity, the metabolic state [20-22]. First, we tested whether movement encoding by HONs depended on fasting state, which is known to strongly modulate HONs[20, 46]. We found that correlations of HON activity and movement were not significantly different in *ad-libitum* fed, 18h-fasted then re-fed, and 18h-fasted mice (Figure 6A). Second, we sought to quantify how the HON movement encoding compares to the recently-described HON encoding of lower-frequency blood glucose information, namely the negative relations between HONs and first temporal derivative of blood glucose[23]. Using a small number of mice from this pre-existing dataset [23] in which video recordings were also available (Figure 6B), we again performed an EMD to align individual HON IMFs to both movement and the first derivative of blood glucose after intragastric infusion of glucose (0.24 g/mL, 900 µL over 10 minutes; Figure 6C). To explore and formally define the HON signal frequency bands that carry information about movement and blood glucose, we fit each HON IMF using a multivariate model with glucose derivative

and movement as weighted predictors of each IMF. We plotted the two fitted weights against corresponding IMF frequency (Figure 6D). Large negative weights for the blood glucose derivative were assigned to lower frequency IMFs, while large positive weights for movement were assigned to higher frequency IMFs (Figure 6D). When binning across frequencies, statistical comparison of these weights indicated that movement had significantly different weights than glucose derivative both in the 0.1 to 0.01 Hz and <0.001 Hz frequency bands (Figure 6E). Notably, glucose derivative did not have significant weights in the higher frequency band, whereas movement did; conversely, movement did not have significant weights in the lower frequency band, whereas glucose derivative did (Figure 6E). Overall, these data indicate that movement representation in the HON population signal is spectrally orthogonal to fasting state or blood glucose dynamics, and is carried selectively in the high-frequency (0.1-0.01 Hz) band of the signal, while glucose information is contained in lower frequency (<0.001 Hz) band (Figure 6F). Finally, we examined if movement encoding by HONs changed as a function of the blood-glucose percentile. By examining the interaction term from linear regressions fit to the n = 6 mice, we observed that movement encoding by HONs was broadly independent of blood glucose percentile (Figure 6G).

Outside of metabolism, it has long been known that HON activity co-varies with arousal [47 48]. We therefore wondered how HON movement encoding compares to their encoding of arousal. To explore this, we quantified arousal by tracking pupil size (an established metric of arousal in both mice and humans [49, 50]). In these recordings we also quantified ocular movements. We then performed multivariate analysis to disentangle and compare statistical contributions of arousal vs body and eye movements to HON activity (Figure 7A). In confirmation of previous results [51], simple regression confirmed that pupil size was positively correlated with HON activity (Figure 7B, r = 0.45 ± 0.08). Ocular movements had a smaller, but still positive correlation (r = 0.26 ± 0.02). Using drop-one feature analysis on a partial least squares regression, we found movement was the most important (highest % contribution) feature to predicting HON activity in our experimental setup (Figure 7C). Expanding this analysis across the frequency domain, an empirical mode decomposition of HON activity revealed that pupil size was maximally encoded at a lower frequency than body movement (Figure 7D-E). In contrast, ocular movements were encoded at a higher frequency than body movement. Overall, these results suggest that HON encoding of movement is distinct from their encoding of pupil-linked arousal.

Movement tracking in HON versus other genetically-defined subcortical neural populations

Finally, we sought to contrast the movement encoding in the HON population against other genetically defined subcortical neural clusters. We selected dopaminergic neurons of the SNc, glutamatergic neurons of the medial vestibular nucleus (MVe), and noradrenergic neurons of the LC, due to their links to HON and previously proposed roles in movement and/or arousal [52-57]. Additionally, we examined SF-1 expressing neurons in the ventral medial hypothalamus (VMH), which are thought to be sensitive to metabolic state [58-62]. We used different BL/6J-derived mouse cre-lines to express cre-dependent GCaMP6s activity indicators in each of these neural clusters, obtaining simultaneous fiber photometry neural activity and body movement recording in each mouse group, in the same way as for HONs (Figure 1A). We found that, like HONs (LHA^{ORX}, r = 0.68 ± 0.04), the MVe glutamatergic neurons (MVe^{GLUT}, r = 0.70 ± 0.06), correlated with movement across the entire recording (Figure 8C). The strength of the correlation was not significantly different across these two populations (p= 0.8366). In contrast, LC^{NA} had only weak positive correlation (r = 0.23 ± 0.07), while SNc^{DA} had a weak negative correlation (r = -0.28 ± 0.08). VMH^{SF-1} neurons had only a slight positive trend (r = 0.20 ± 0.11). Cross correlation between GCaMP6s and the movement metric showed that HON activity on average preceded movement by a few samples (-0.34 ± 0.12 seconds), as did the LC^{NA} and SNc^{DA} (-0.72 ± 0.15 and -1.08 ± 0.52 seconds, respectively). MVe^{GLUT} activity was closely aligned to movement (-0.15 ± 0.09), and VMH^{SF-1} activity followed movement by several seconds (4.23 ± 0.15) using the 1.5× inter quartile range to filter for outliers (Figure 8D). We then repeated the clustering analysis described in Figure 4, aligning the photometry signals to initiation of movements assigned to "small" or "large" movements (Figure 8E). For large movements, HON activity encoded movement similarly to MVe^{GLUT} neurons (p = 0.3915, Figure 8G). However, for small movements, HON activity encoded the movement metric significantly better than MVe^{GLUT} neurons (p = 0.0099, Figure 8G). Together, these data suggest HONs are uniquely positioned to track body movement to a degree not observed in the other subcortical populations we examined.

Discussion

We found that, across behaviors, HONs tracked the amount of body movement with a high degree of precision. This tracking occurred in a higher frequency bandwidth than their tracking of blood glucose, contributing to effective multiplexing of these two fundamental physiological variables. The HON movement tracking was not significantly different across hunger and glycemic states, suggesting orthogonal multiplexing of the movement and energy states. At two key projection targets of HONs, orexin/hypocretin peptide output was also related to movements, but in a projection-specific way, implying a heterogeneity in the movement-related HON outputs. Among the multiple neurochemically-defined subcortical neural clusters examined here, HONs were dominant in the precision of their movement tracking.

What would be the evolutionary advantages of coupling body movement to proportional changes in HONs? A central hypothesis for the meaning of HON activation is increased arousal, with evidence including electroencephalography [26], pupil dilation [50, 51], and cardiorespiratory adaptations [63 64-66]. Though our projection-specific data imply that there may be subsets of HONs that are negatively related to movement (Figure 5), at the HON population level overall the coupling between neural activity and movement was positive (r=0.68, Figure 1). A simple interpretation of these data is that, via the HON movement tracking, the brain creates a "wake up" signal in proportion to movement, which could be helpful since dealing with challenges and opportunities created by movement may benefit from increased arousal. Importantly, HONs are also implicated in the mobilization of body glucose stores and shuttling glucose from liver to muscle [67]. Multiplexing their activation to both movement and glucose-sensing may allow movement process to be optimally matched to movement energy demands.

It is tempting to speculate on the breadth at which HON population activity encodes physiological derivatives (i.e. rate-of-change in physiological parameters) multiplexed across the frequency domain. This study highlights how HONs represent instantaneous movement magnitude, which can be rephrased as a change in body position over time. Similarly, we previously reported population HON activity predominantly tracks the derivative of blood glucose, rather than proportionally encode glycemic state [23]. Knowing the rate at which a physiological variable is changing allows for anticipatory responses, such as in Proportional-Integral-Derivative (PID) sensorimotor control loops, where the derivative-control component enables adaptive prediction of erroneous deviations from a set-point [68, 69].

Do HONs "read" or "write" movements? From the perspective of sensorimotor control loops, the answer should be both. In theory, HONs could "read" movements either by sensing them, or by receiving efference copies and/or corollary discharges corresponding to motor commands[70]. Prior studies indicate that acute, targeted HON stimulation can evoke or modulate certain kinds of movement [71-74]. Orexin receptor antagonism – or optogenetic suppression or deletion of HONs – evoked either locomotor suppression or no effect on locomotor parameters [75-77], consistent with our present result that the power-frequency spectrum of movements was not strongly dependent on presence of HONs themselves (Figure 4). Our finding that orexin level in the SNc – a site where orexin stimulates locomotion [23] – is higher before movements rather than during movement (Fig. 5) also suggest that at this site, orexin may be more involved in movement initiation rather than maintenance. Interestingly, in the LC, the opposite orexin profile is seen (Fig. 5); given the role of LC in arousal, this may mean that orexin in the LC provides increased arousal during ongoing movement. Overall, it terms of movement control, HONs may be sufficient to "write" movements, but they are not necessary. Furthermore, it is tempting to speculate on the implications of HON loss-of-function viewed from the lens of a sensorimotor control loop. Without derivative-control, a system is still able to measure and perturb a variable, however its ability to dampen unwanted oscillations from a set-point is strongly impaired. From this perspective we can speculate that narcolepsy-cataplexy, caused by HON loss-of-function, is perhaps explained by oscillations into unwanted sleep-states and motor programs due to impaired control loops for wakefulness and movement.

In addition to these fundamental implications, there is an applied implication of our findings for basic neuroscience research. Ever since the importance of HONs for brain function and brain-body coordination was

established [24, 25, 31, 78], a demand appeared for tracking their function across research and clinical settings, and many useful (but invasive) techniques for this were developed [40, 45, 47, 48, 79]. The high correlation between body movement and HON activity demonstrated here suggests that video-tracked pixel difference could serve as a simple non-invasive biometric for real-time estimation of HON population state, at least as validated here in head-fixed behaving mice, a widely used model in neuroscience research [80, 81], where assessment of arousal-linked signals is in continuing demand [15, 82-84 85, 86].

Our results open multiple directions for further study. Upstream of HONs, it would be important to solve the challenging puzzle of how movement information is conveyed to these neurons. This challenge may likely require an extensive functional screen, because of the wide-spread monosynaptic inputs to HONs, with many of these coming from areas where some movement-associated activity has been reported [87]. Within the HON population activity studied here, individual cells and their possibly heterogeneous responses to movement also remain to be defined, since the present results likely represent only a dominant subpopulation of HONs. Downstream of HONs, the findings in Figure 5 could be extended to probe the role in movement communications of the multiple transmitters released by HONs[88-90] to the genetically-distinct, brain-wide targets of their terminal projections[29]. In future work, it will also be important to test whether movement tracking by HONs is used for optimal adjustments of the many cognitive and autonomic processes linked to HON outputs.

In summary, our findings define a key aspect of brain activity that is rapidly and precisely synchronized to even small alterations in body movement. The brain needs to sense movement for predicting future states and energy needs. Our results show that movement is encoded in parallel within glycemic state within different frequency domains of HON activity, presumably allowing these cells to communicate both energy supply and a key aspect of energy demand in the body. Deeper insights of how defined neurons and connection turn body movement into adaptive responses will enable insights into the impact of body movement on brain function in health and disease.

Materials and Methods

Experimental Subjects

All animal experiments followed the Swiss Federal Food Safety and Veterinary Office Welfare Ordinance (TSchV 455.1, approved by the Zürich Cantonal Veterinary Office). Adult C57BL/6J-derived lines were studied. We used previously validated cre-dependent transgenic mice: Vglut2-ires-Cre (Slc17a6$^{tm2(cre)Lowl}$/J, JAX:016963), SF1-Cre (Tg(Nr5a1-cre)7Lowl/J, JAX:012462), DAT-Cre (*Slc6a3*$^{tm1(cre)Xz}$/J, JAX:020080), or DBH-iCre (C57BL/6-Tg(Dbh-icre)1Gsc, MGI:4355551, [91]). For HON ablation experiments we used the previously validated orexin-DTR mice, wherein all HONs were ablated via injection with diphtheria toxin >2 weeks before experiments began [40, 41]. All mice were male except for a small number of Vglut2-ires-Cre and DBH-iCre mice, which were similar to males and therefore pooled. Thus, whether all conclusions apply to female mice remains to be determined. Animals were housed in a 12:12 hour light-dark cycle and had *ad libitum* access to water and food (3430 Maintenance Standard diet, Kliba-Nafag) unless stated otherwise. All experiments were performed in the dark phase. Studies were repeated in at least two independent cohorts and, when relevant, used a semi-randomized crossover design for fasting state.

Surgeries and Viral Vectors

To record photometry across a range of brain regions, we stereotaxically injected viral vectors into adult mice as follows. In all cases, mice were anesthetized with 2-5% isoflurane following operative analgesia of buprenorphine and site-specific lidocaine. Viruses were stereotaxically injected at 1-2 nL/s (NanoInject III injector) either unilaterally, or bilaterally, at the following coordinates relative to bregma: anteroposterior (AP), mediolateral (ML), and dorsoventral (DV).

The previously validated promotor-driven AAV1-hORX-GCaMP6s.hGH [40] ($2.0x10^{13}$ GC/mL, Vigene Biosciences) was used to record from HONs in the **LHA:** AP -1.35, ML ± 0.95, DV -5.70, -5.40, and -5.10 mm. 70 nL per site. For cre-dependent mouse lines, we injected AAV9.CAG.Flex.GCaMP6s.WPRE.SV40, a gift from Douglas Kim & GENIE Project (Addgene plasmid # 100842; $1.9x10^{13}$ GC/mL, 1:5 dilution in sterile PBS) in the **MVe:** AP -6.05, ML ± 0.95, DV -4.40 mm. 200 nL per site. In the **VMH:** AP -1.35, ML ± 0.45, DV -5.75, -5.50, and -5.25 mm. 70 nL per site. In the **SNc:** AP -3.20, ML ± 1.40, DV -4.20. 200 nL per site. In the **LC:** AP -5.35, ML ± 0.90, DV -3.70 and -3.50 mm. 100 nL per site. The orexin-sensor, AAVDJ.hSynapsin1.OxLight1 ($7x10^{12}$ GC/mL, UZH Viral Vector Facility, 1:3 dilution in sterile PBS) was injected into both the SNc or LC at the above coordinates. 150 nL per site. Optic fiber cannula of 200 um diameter, 0.39 numerical aperture (NA) with a 1.25 mm ceramic ferrule (Thorlabs) were implanted 0.1 mm above the most dorsal injection site. A custom-made aluminum head-plate was secured to the skull using dental cement (C&B Metabond). Mice were given postoperative analgesia and allowed to recover for at least two weeks before the first experiment.

Expression was confirmed experimentally by observing dynamics at 465 nm excitation. A small number of mice without any observable dynamics at 465 nm, or with strong artifacts in the 405 nm isosbestic, were excluded from analysis. Expression was additionally confirmed terminally, via perfusion with 4% PFA in sterile PBS, histological slicing, and then imaging with a fluorescence microscope (Nikon Eclipse Ti2). For histological confirmation of the orexin-DTR mice, HONs were labeled with goat anti-orexin A (1:250 dilution, sc-8070 Santa Cruz Biotechnology) followed by and donkey anti-goat Alexa-546 (1:500 dilution, A11056 Invitrogen) and a Hoechst stain.

For intragastric infusion surgeries as in Figure 6, a small number of experiments from Viskaitis et al. 2024 were re-analyzed if video was also available, the detailed methods for these glucose experiments are given in this source publication [23].

Fiber Photometry

For fiber photometry, we used a custom-build camera-based photometry system. GCaMP6s (or OxLight1) activity was recorded at 10-20 Hz via alternating excitation between 405 nm and 465 nm LEDs (Doric; average

power 20 µW at fiber tip) in multiple animals simultaneously. The 405 nm excitation was used as an isosbestic control for movement artifacts. Most recordings were either 20 or 40 minutes long, except in Figure 6 when recording lasted for >1 hour. The first minute of each photometry trace was removed due to bleaching artifacts. Further 465 mm fluorescence bleaching was accounted for by subtracting a triple exponential curve fit to the trace. Finally, each trace was z-score normalized to its standard deviation and mean. For visual clarity only, photometry traces in Figure 1D, Figure 5A, Figure 7B, and Figure 8A were smoothed using a 1-second moving average filter; all statistical comparisons and derived metrics were calculated using raw data. **Movement Metrics**

All experiments were performed in a closed container illuminated via infrared LEDs to achieve constant luminance during the recording. The movement metric was generated from videos captured using a commercial infrared camera (Blackfly S USB3, Teledyne FLIR) at the same sampling rate as photometry (10-20 Hz). To generate the metric, per-pixel differences were calculated across consecutive frames with 8-bit resolution. Then, the absolute value of the difference across every pixel was summed for each consecutive frame to generate one value for each sample, excluding the first frame. To compare this movement metric to concurrently measured photometry, the resulting trace was convolved with a "GCaMP6s kernel" which consisted of a 60 second exponential decay kernel with a decay rate equivalent to the reported GCaMP6s half-life (1.796 s [38]). Then, the first minute of convolution was removed to match the photometry trace and the resulting trace transformed to a z-score using its standard deviation and mean. To calculate the correlation between the movement metric and photometry, we aligned all samples from both outputs across the entire recording period, then calculated a pearson's r (scipy.stats.pearsonr, SciPy v1.14.0). Pearson's r results were averaged per-mouse across repeated recording sessions. When relevant, locomotion-specific motion was recorded using an optical encoder (Honeywell, 128 ppr 300 rpm Axial) and digital acquisition box (BNC-2110, National Instruments). Locomotion was filtered using a 5-sample (250 ms) moving average filter for visualization only.

For bout-related analyses, we detected movement-bouts by first smoothing the z-scored movement-metric with a 20-sample (1 second) moving average filter and then aligning to sample indices where movement was < 0 SD for at least 4 seconds before exceeding the threshold. For subsequent clustering, a K-Means algorithm (scikit-learn) in the default configuration was implemented to identify k = 2 clusters of movement from the identified bouts. Photometry signals were aligned to bout indices then baselined by calculating a z-score of 1-3 seconds before bout initiation.

Pupillometry

Pupil dynamics were recording using a separate infrared camera (Blackfly S USB3, Teledyne FLIR) at a frame rate synchronized to photometry and the body-movement camera at 20 Hz. To calculate pupil metrics, we used a standard DeepLabCut [92, 93] 3.0 pipeline and manually labeled 405 video frames to identify eight points surrounding the edge of the pupil. A model was fit following 5-percent holdout validation using default recommended DeepLabCut parameters for a pretrained ResNet50 [94]. Briefly, the model was trained over 200 epochs from a starting learning rate of 1×10^{-4} using the Adam optimizer. The learning rate decreased by a factor of ten at epoch 160 and again at 190, following the default scheduler. After the model fit, we extracted pupil coordinates from all videos and manually inspected for accuracy. Using python, we fit a circle (scipy.optimize.minimize, method="Nelder-Mead") to all points which DeepLabCut assigned a confidence above 0.8. During blinking, or when DeepLabCut did not return a confidence of 0.8 for at least 3 points, pupil size was linearly interpolated. Pupil size was defined as the area of the fitted circle. Ocular movements were defined as displacements of the fitted circle's center. Pupil size and ocular movements were then z-scored to the mean and standard deviation of the entire trace.

Concurrent monitoring of glucose and intragastric infusions

The HD-XG telemetry system (DSI) as described in Viskaitis et al. 2024 was used to measure and preprocess blood glucose concentrations as per manufacturer instructions. For intragastric (IG) glucose infusions, 900 µL 0.24g/mL glucose dissolved in sterile saline was infused at a rate of 90 µL/minute for 10 minutes. Saline

controls are shown in the source publication and did not perturb HONs[23]. Missing samples were linearly interpolated, and the resulting glucose trace was resampled (scipy.signal.resample) to align to the photometry recording Hz. To generate the derivative traces, the raw glucose trace was smoothed using a 10 minute moving average filter then resampled to align to the photometry recording Hz before the first derivative was calculated.

Empirical mode decomposition

The logic of empirical mode decomposition analysis was largely based on [95], and was performed using the default settings of the python EMD toolbox version 0.6.2 [96]. Briefly, traces were first normalized (z-score) before IMFs were calculated using the sift algorithm [39]. The instantaneous phase, amplitude, and frequency across each IMF were calculated using the Normalized Hilbert Transform Method. The characteristic frequency was determined by taking the mean of each IMF's frequency data weighted per-sample by the IMF's amplitude data. Extremely low-frequency ($< 10^{-3}$ Hz) IMFs were excluded as they did not complete enough cycles to allow sufficient sampling for the following statistics. Power was taken as the means of the squared amplitude data and expressed as a percentage of the total power from each IMF. The preferred phase (direction) and coupling strength (length) for each IMF's phase data was then calculated from the 1st trigonometric circular moment with weights corresponding to positive ("active") or negative ("quiescent") signed samples of the movement metric. Note that in the "active" case, for example, all negative values of the movement metric would be assigned weights of zero.

Behavioral classification

To classify behaviors, we used the video captures and manually labeled five behavioral classes: chewing, grooming, resting, running, and sniffing, from greyscale frames using the previous, current, and subsequent frames to form an RBG input image. 4'221 manually labeled frames were split into a "train" and "test" datasets, stratified across behavioral classes, following ten-percent holdout validation. When generating the datasets, we augmented the dataset using random horizontal and vertical flips of the input frames, to ensure robustness of the behavioral classification. A convolutional neural network was constructed using PyTorch 2.2.0: we used the standard ResNet18 with pretrained weights on the ImageNet dataset as previously described [94], but with a final linear layer corresponding to the five output classes. To train the model, we used an Adam optimizer with an initial learning rate of 1×10^{-4}, and a cross entropy loss function. A scheduler (torch.optim.lr_scheduler.StepLR) decreased the learning rate by a factor of 10 every 10 epochs. The model was fit on 41 total epochs using a Tesla T4 GPU (NVIDIA) using a batch size of 128. The model was independently fit several times and consistently achieved over 98.6% accuracy on the "test" dataset, with a cross entropy loss of < 0.054 . The trained network was then used to classify photometry-synchronized videos. The model output was passed through a softmax function, and thereby consisted of n video-frames x 5 behavioral likelihoods. We smoothed the model-predicted likelihoods for each behavior using a 4-second moving average filter and took the max-likelihood behavior at each frame as the assigned classification. Finally, the videos and predictions were manually inspected for accuracy.

Data analysis and statistics

Raw data were processed with custom scripts in Python 3.9, using Seaborn and Matplotlib libraries for plot-generation. Statistical analysis was similarly performed in Python using Pinguoin v0.5.4, SciPy v1.14.0, and scikit-learn 1.2.1 libraries. In Figure 2 and 3, local regressions were performed using statsmodels v0.14.1 with a 0.3-0.5 fraction of the data. Confidence intervals were generated using 1000 bootstrapped samples. In the case of strictly positive variables (% power), we used a logarithm link function and transformed the result back into its original units for visualization. Circular regressions were similarly performed using scikit-learn and a multi-output support vector regression whereby the phase (θ) in radians was evaluated over 7 evenly spaced samples on the log-scale frequency by converting the phase into a multidimensional vector y:

$$y = [\sin(\theta), \cos(\theta)]$$

Linear mixed effects models in Figure 2E were used to predict z-scored GCaMP6s photometry using the z-scored movement metric or behavioral classification. Models were defined as follows:

$$Model\,1, \qquad GCaMP6s_{ij} = \beta_0 + \beta_1 \times C(Behavior)_{ij} + b_{0i} + \epsilon_{ij}$$

$$Model\,2, \qquad GCaMP6s_{ij} = \beta_0 + \beta_1 \times Movement_{ij} + b_{1i} \times Movement_{ij} + \epsilon_{ij}$$

$$Model\,2, \qquad GCaMP6s_{ij} = \beta_0 + \beta_1 \times Movement_{ij} + b_{1i} \times Movement_{ij} + \beta_1 \times C(Behavior)_{ij} + b_{0i} + \epsilon_{ij}$$

Where $GCaMP6s_{ij}$ is the photometry sample, $C(Behavior)_{ij}$ is the behavioral classification, and $Movement_{ij}$ is the movement metric for the *j*-th observation of the *i*-th mouse. β_0 is the intercept, and β_1 and β_2 are the fixed effects. b_{0i} is a random intercept of the *i*-th mouse. b_{1i} is the random slope for movement of the *i*-th mouse. ϵ_{ij} is the residual error. We assumed the residual error was normally distributed.

Linear regression models for Figure 6 were calculated using the statsmodels library following the formula:

$$IMF_n = \beta_0 + \beta_1 X_1 + \beta_2 X_2 + \epsilon$$

Where IMF_n is the nth IMF of the GCaMP6s signal, β_0 is the intercept term, β_1 and β_2 are the coefficients for X_1, blood-glucose derivative, and X_2: movement metric, respectively, and ϵ is the error term.

Partial least squares regressions in Figure 7 were calculated using scikit-learn with n = 2 components. To perform drop-one feature analysis[97], the movement metric, pupil size, and ocular movements were used as predictors to generate a "full model." The generated R^2-score (calculated as the average of a 5-fold cross validation) is denoted as R^2_{full}. The predictors were then removed from the model one at a time, and a "partial" $R^2_{partial}$ was generated. The contribution of each predictor *k* was therefore defined as:

$$\%\,Contribution_k = 100 \times \left(1 - \frac{R^2_{partial,k}}{R^2_{full}}\right) \Big/ \sum_{j=1}^{3} \left(1 - \frac{R^2_{partial,j}}{R^2_{full}}\right)$$

Statistical tests, sample sizes, and their results are indicated in the figures, legends, and/or descriptions in the text. Where significance is presented, p-values are as follows: *p<0.05, **p<0.01, ***p<0.001, and ****p<0.0001, n.s. p>=0.05. We made no assumptions regarding the directionality of our effects; all statistical tests were two-tailed. When relevant, multiple comparisons adjustments were made using the Bonferroni correction as indicated in figure legends / or text. Data are presented as means and standard error of the mean (SEM) unless stated otherwise. Boxplots always represent the maximum, minimum, interquartile range, and median of the data.

Conflict of interest statement

The authors declare no competing financial interest.

Acknowledgements

This work was funded by ETH Zürich. DB and ALT conceived the study and designed the protocol, with contributions from PV. ALT, PV, NG, DD, and EB performed the surgeries. ALT and PV performed most of the experiments. ALT designed and performed data analyses with contributions from PV and DD. TP provided and advised on the orexin sensor. DB and ALT wrote the text with inputs from DPR and NG. The authors have no competing interests to declare.

Data availability

Source data has been deposited in a publicly available database (https://osf.io/6d45m/).

Figures and Legends

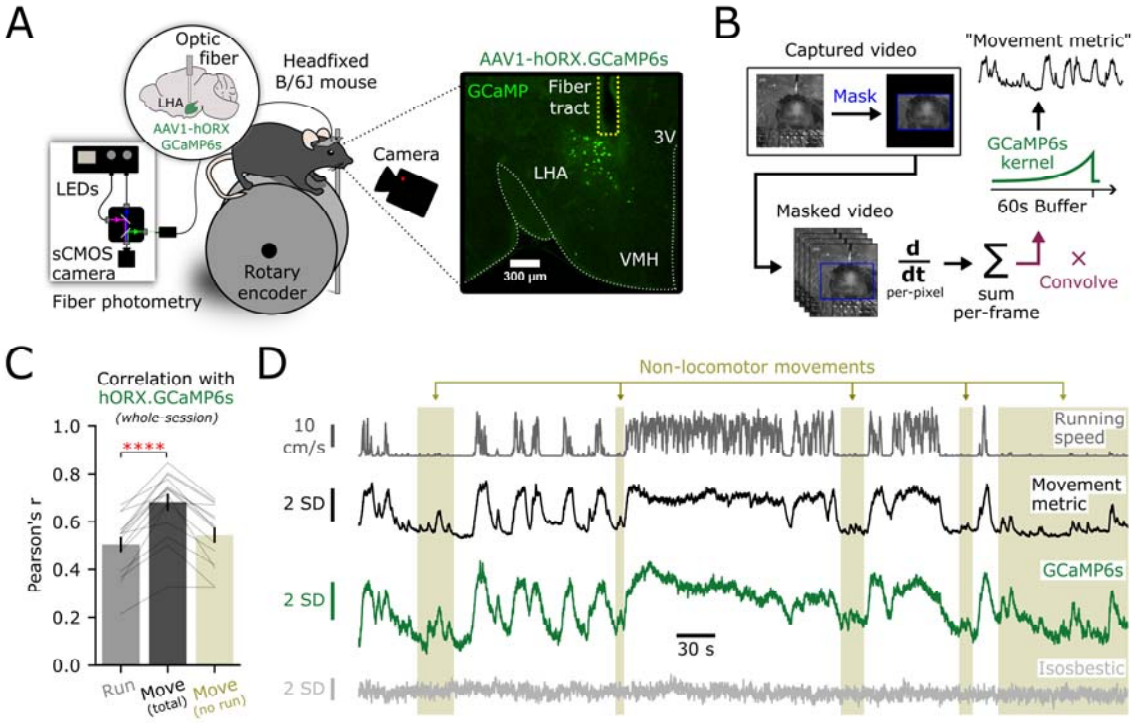

Figure 1. Movement magnitude is represented by rapid HON dynamics.

A, Schematic depicting the photometry system and voluntary wheel-running apparatus with video capture (left) and representative expression (right) of AAV1-hORX-GCaMP6s in HONs. LHA; lateral hypothalamic area; 3V; third ventricle; VMH; ventral medial hypothalamus. ***B,*** Processing pipeline to generate a "movement metric" from video recording of voluntary movement. ***C,*** Whole-session correlation of HON photometry with simultaneously recorded behavior metrics from n = 15 mice: running (r = 0.50 ± 0.03), the movement metric (r = 0.68 ± 0.04), the movement metric in epochs where locomotion was < 1 $cm{\cdot}s^{-1}$ (r = 0.54 ± 0.03). Metrics given as mean ± SEM, connected lines represent individual mice. Asterisks indicate comparison between running and movement metric (paired *t*-test: t_{14} = 6.676, **** p < 0.0001). ***D,*** Traces from an example experiment. From top to bottom: running on the wheel, the video-derived movement-metric, HON GCaMP6s photometry, and isosbestic control. Shaded beige regions indicate non-locomotor epochs where the movement metric still reported strong positive correlations with HON activity.

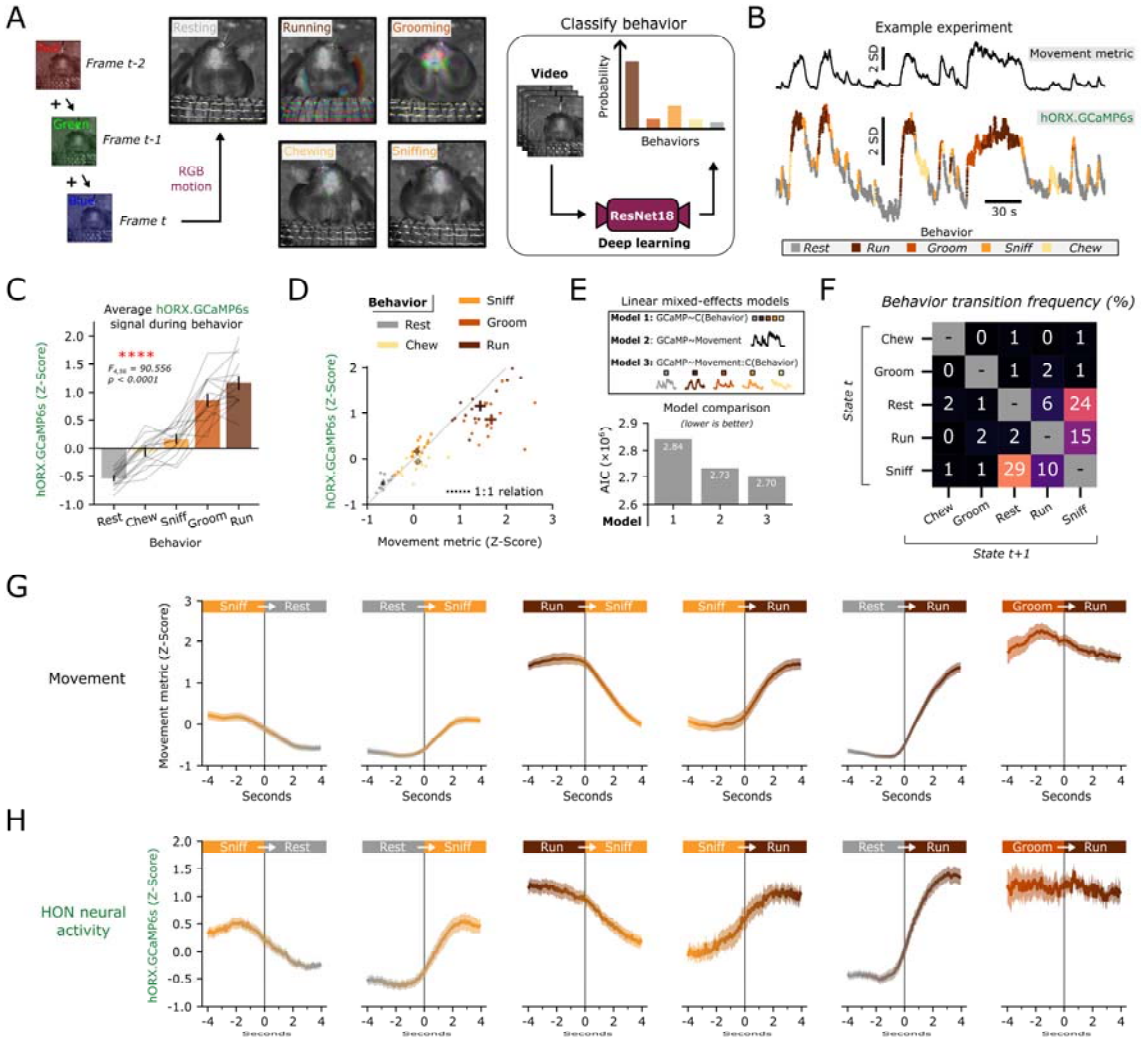

Figure 2. HON dynamics represent movement magnitude across classified behaviors.

A, Diagram for classifying behaviors from video recordings via deep learning. ***B,*** Example experiments showing movement (upper, black) and color-coded photometry (lower) after behavioral classification. ***C,*** Average normalized HON GCaMP6s signal across classified behaviors in n = 15 mice (rmANOVA: $F_{4,56}$ = 90.556, **** p < 0.0001). ***D,*** Average value of the normalized HON GCaMP6s signal from n = 15 mice plotted against the average value of the movement metric in each classified behavior. Thick bars represent SEM across both metrics. The dotted line represents an idealized 1:1 linear relationship between movement and photometry with an intercept at zero. ***E,*** Comparison of three linear mixed effects models using movement and/or behavioral classification to predict HON GCaMP6s signal, quantified by Akaike information criterion. ***F,*** Average behavioral transition matrix for n = 15 mice. ***G,*** Average movement metric aligned -4 to +4 seconds from a behavioral transition. The six most frequent behavioral transitions are plotted. Lines and shaded region represent mean and SEM. ***H,*** Same as G, but with hORX-GCaMP6s signal.

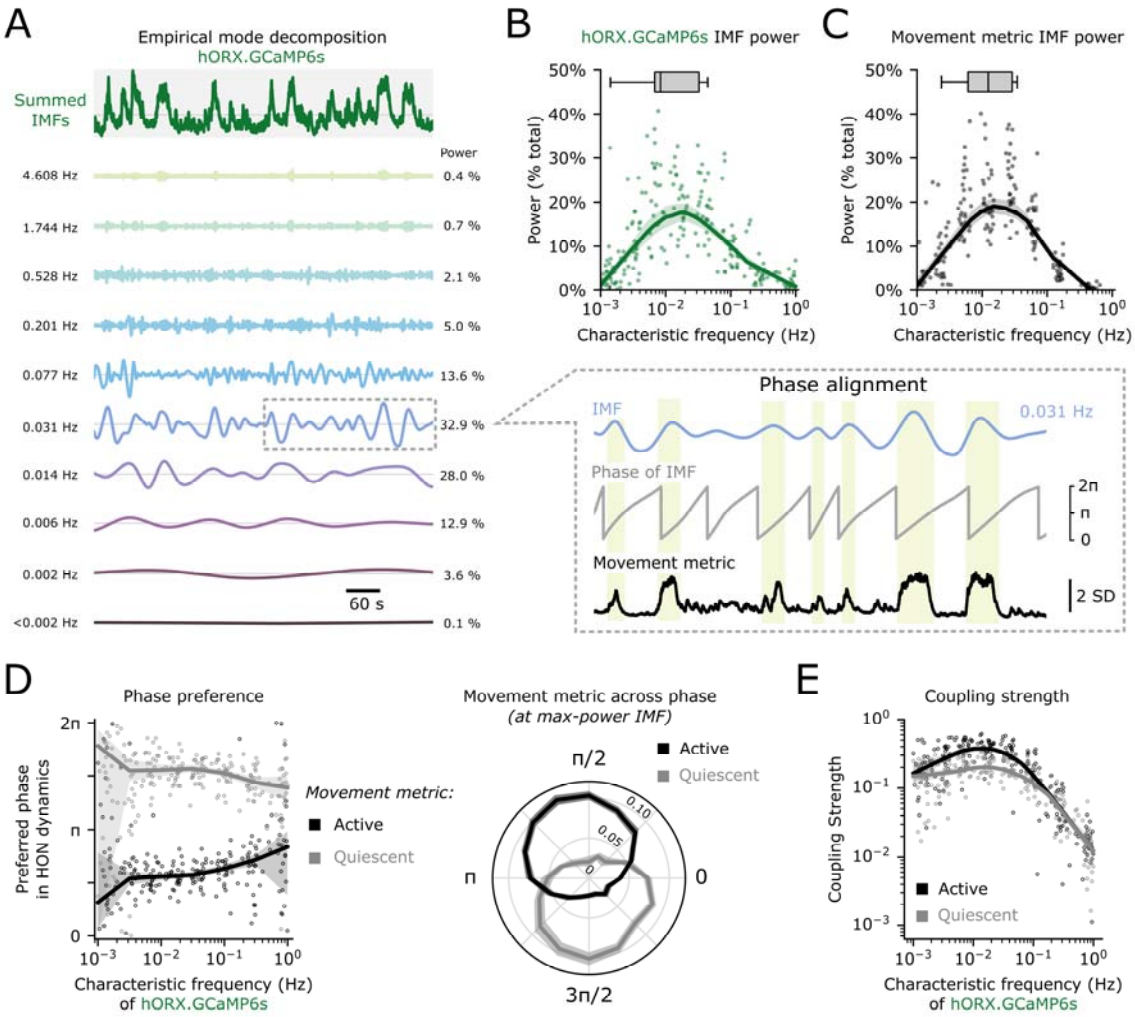

Figure 3. Movement magnitude is phase-aligned to HON activity across the frequency domain.

A, Representative empirical mode decomposition (see methods) of HON GCaMP6s activity from one experiment. The top green trace displays a summation of all IMFs. Below are the first 10 IMFs sorted by characteristic frequency in Hz. Relative power is reported as a percentage of the total. Dashed grey box (middle right) represents a cutout of the 0.031 Hz IMF in which movement epochs (shaded beige regions) are clearly phase-aligned in the 0-π period. ***B,*** Average power plotted against characteristic frequency of n = 229 GCaMP6s-derived IMFs derived from 27 experiments using 15 mice. Thick line and shaded region represent a local regression and 95% CI. Boxplots represent the maximum power IMF from each experiment. ***C,*** Same as B, using n = 214 movement metric-derived IMFs. ***D,*** Left: Preferred phase of both active (black) and quiescent (grey) epochs of the movement metric plotted against characteristic frequency. Dots represent n = 229 GCaMP6s-derived IMFs derived from 27 experiments using 15 mice. Thick line and shaded region represent a circular regression and 95% CI. Right: average absolute value of the z-scored movement metric plotted on the radial axis against the phase of the maximum-power IMF. Lines represent mean ± SEM from n = 15 mice. ***E,*** Coupling strength of the movement metric to GCaMP6s IMFs in both active (black) and quiescent (grey) epochs plotted against the IMF's characteristic frequency. Dots represent n = 229 GCaMP6s-derived IMFs derived from 27 experiments using 15 mice. Thick line and shaded region represent a local regression and 95% CI.

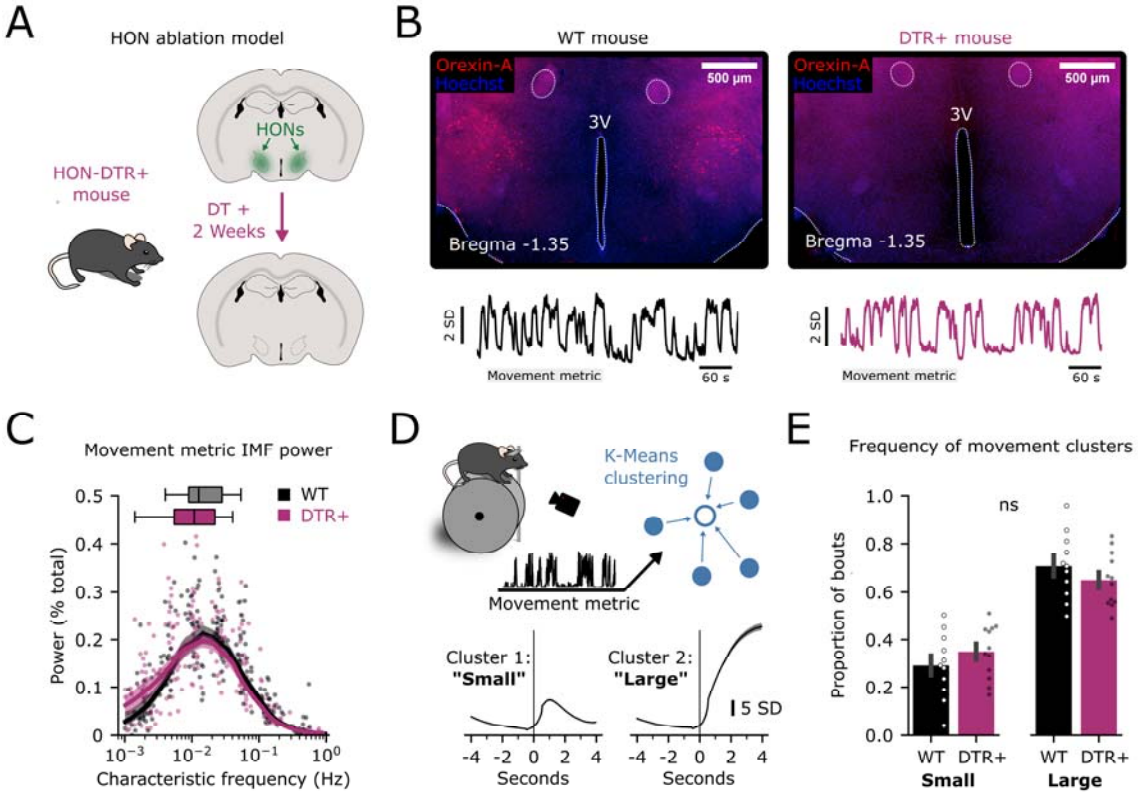

Figure 4. HONs are not required to maintain movement profiles.

A HON ablation in HON-DTR+ mice. ***B,*** Brain slice histology of a wild-type mouse (WT, left, image representative of n = 11 mice) and a HON-ablated mouse (DTR+, right, image representative of n = 12 mice) stained for OrexinA (red). 3V = 3rd ventricle. ***C,*** Average power plotted against characteristic frequency of movement metric-derived IMFs (WT: n = 217 IMFs from 30 experiments using 11 mice. DTR+ n = 267 IMFs from 34 experiments using 12 mice). ***D,*** Diagram of K-Means clustering to generate two clusters of movement representing voluntary initiation motion following >4s of no motion, see methods. **E,** Proportion of bouts which were assigned "small" or "large" were not significantly different across genotypes (Unpaired *t*-test, $t = 1.1167$, $p = 0.2767$).

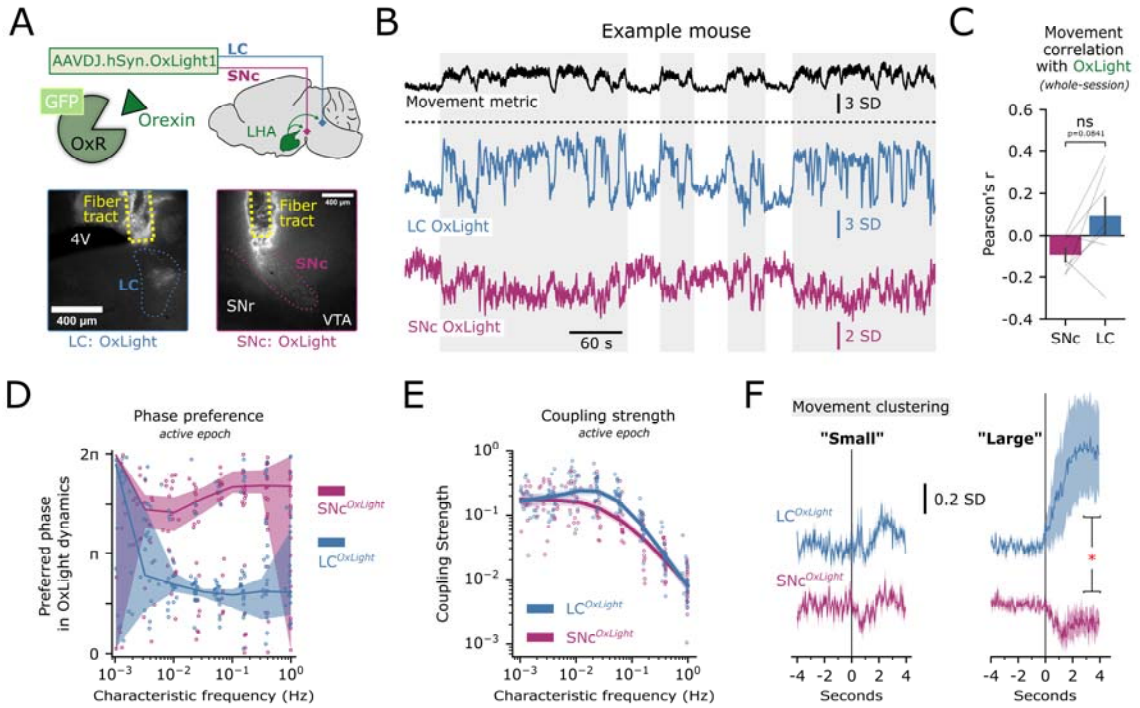

Figure 5. Movement-related orexin peptide release is non-homogenous across projection targets.

A, Schematic representing targeting of the orexin sensor OxLight1 to the LC and SNc, representative histology from n = 7 mice. ***B,*** Example experiment displaying the movement metric and OxLight1 signal in the LC (blue) and SNc (purple) in the same mouse. Shaded regions represent movement epochs. ***C,*** Mouse-averaged whole-session correlation of movement with OxLight1 photometry in the SNc and LC (paired *t*-test: t_6 = 2.068, p = 0.0841). ***D,*** Preferred phase of individual EMD-derived OxLight1 IMFs to active epochs of the movement metric plotted as a function of the IMF's characteristic frequency. n = 317 IMFs from 21 experiments using 7 mice. Thick line and shaded region represent a circular regression and 95% CI. ***E,*** Coupling strength of individual EMD-derived OxLight1 IMFs to active epochs of the movement metric plotted as a function of the IMF's characteristic frequency. n = 317 IMFs from 21 experiments using 7 mice. Thick line and shaded region represent a local regression and 95% CI. ***F,*** Photometry baselined -3 to -1 seconds before movement initiation in two clusters: small movements (left) and large movements (right). Lines and shaded regions represent mean ± SEM of n = 6 mice. Asterisk represents a paired statistical comparison of mean signal 3 to 4 seconds after movement initiation (Wilcoxon test, D_6 = 1.0, * p = 0.03125).

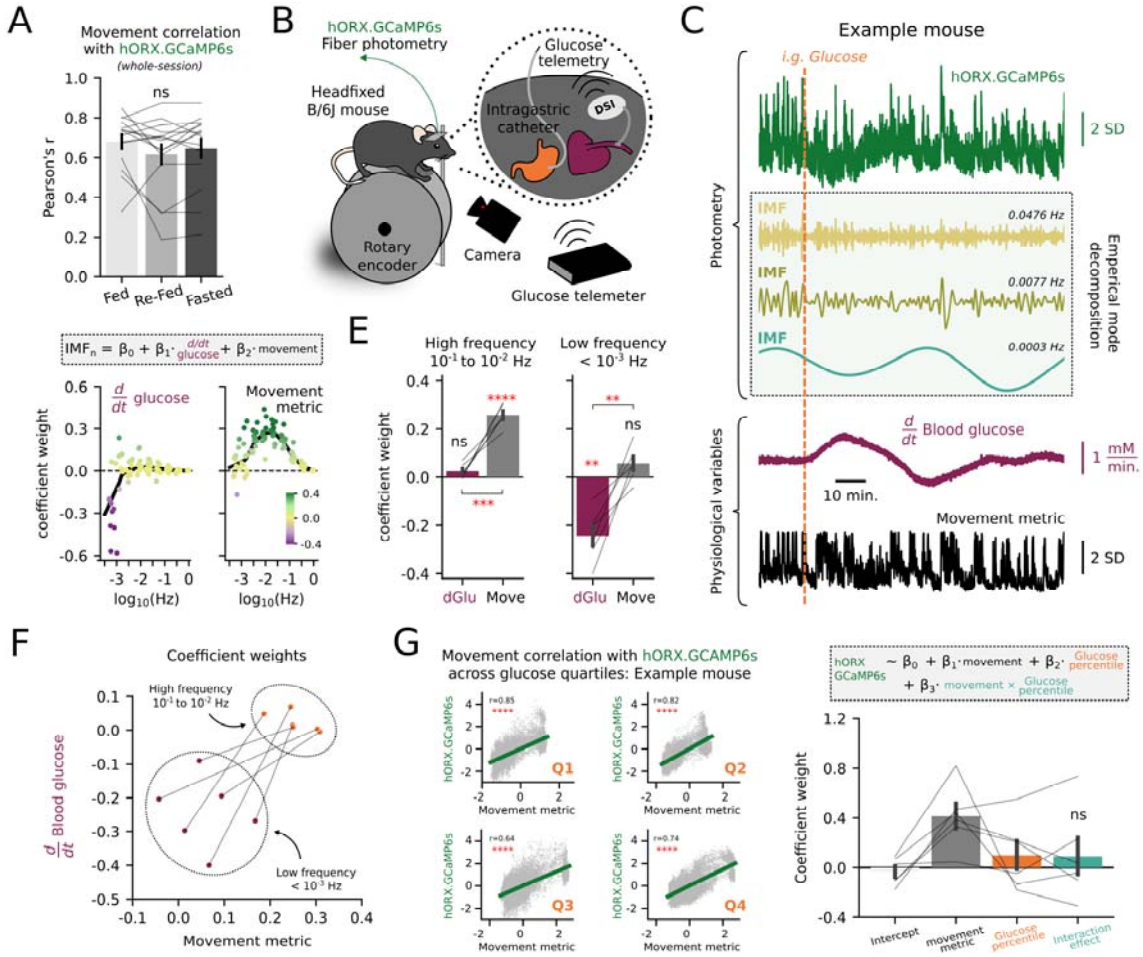

Figure 6. HONs multiplex movement and blood glucose across frequency domains.

A, Correlation of movement with HON photometry across three states of fasting (n = 15 mice). Fed: ad-libitum access to chow. Re-fed: 18-hour fasted and then food returned 2 hours before experiment. Fasted: 18-hour fasted mice (rmANOVA: $F_{2,28}$ = 1.848, p = 0.176). ***B,*** Scheme of experimental setup including photometry, glucose telemetry (DSI), video capture, and intragastric catheter infusions (Viskaitis et al., 2024). ***C,*** Example HON GCaMP6s photometry trace (top), three derived IMFs (middle), and simultaneously recorded physiological variables of blood glucose (plotted as the first derivative) and movement magnitude (lower). A vertical dashed orange line represents an intragastric infusion of glucose. **D,** A linear model was fit to predict n = 94 IMFs using the glucose derivative and movement. Fitted coefficient weights are plotted as a function of the IMF's characteristic frequency. ***E,*** Per-mouse (n = 6) binned coefficient weights. For the higher frequency bin (left, 10^{-1} to 10^{-2} Hz), coefficient weights were tested against a population mean of zero (Bonferroni-corrected one-sample *t*-test: glucose derivative t_5 = 1.965, p = 0.2131; movement t_5 = 14.102 p < 0.0001). Coefficient weights of glucose derivative were compared to movement (paired *t*-test: t_5 = 8.331, p = 0.0004). For the lower frequency bin (right, < 10^{-3} Hz), coefficient weights were similarly tested against a population mean of zero (Bonferroni-corrected one-sample *t*-test: glucose derivative t_5 = -5.631, p = 0.0049; movement t_5 = 1.963, p = 0.2139). Coefficient weights of glucose derivative were compared to movement (paired t-test: t_5 = 5.385, p = 0.0030). Bar plots display mean ± SEM. ***F,*** Alternate visualization of E with coefficient weights plotted against each other. ***G,*** Left: correlations of HON GCaMP6s signal and the movement metric across blood-glucose quartiles in an example mouse. Right: Regression predicting HON GCaMP6s activity using movement and blood-glucose percentile, performed per-mouse (interaction effect; one-sample *t*-test: t_5 = 0.6250, p = 0.5594). Bar plot displays mean ± SEM.

*$p < 0.05$, **$p < 0.01$, ***$p < 0.001$, ****$p < 0.0001$ and ns, not significant by two-tailed tests.

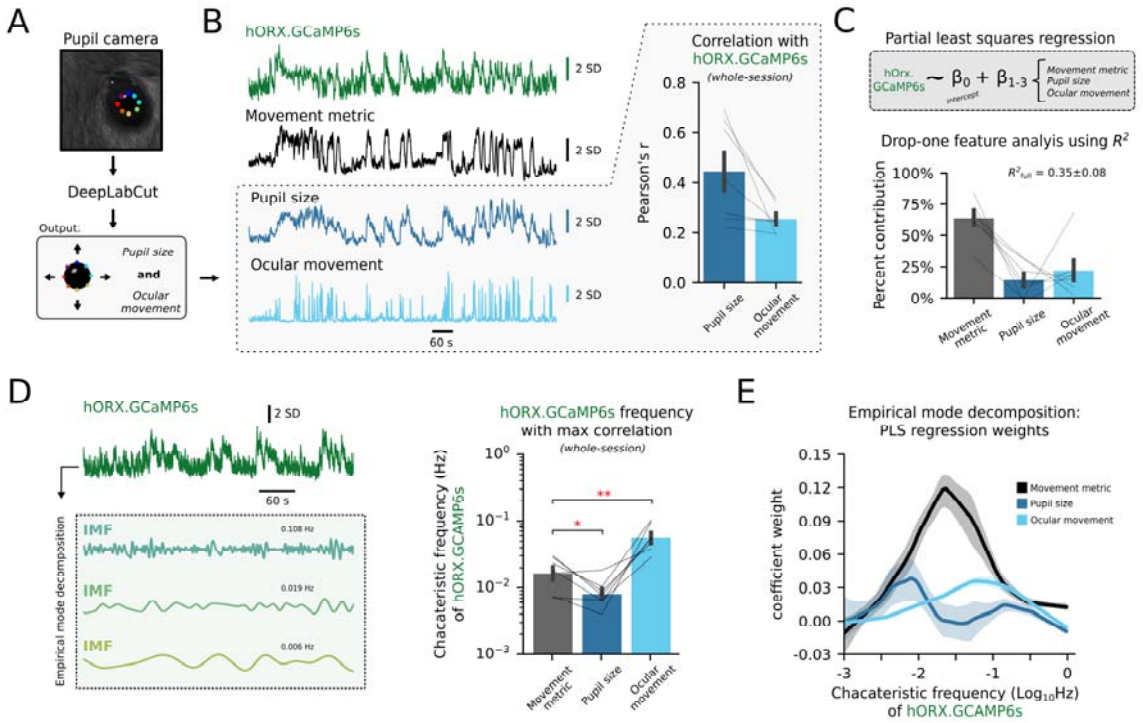

Figure 7. Disentangling contributions of arousal vs movement to HON activity.

A, Scheme of pupillometry processing pipeline. ***B,*** Example aligned recording of HON GCaMP6s photometry (green), movement metric (black), pupil size (dark blue), and ocular movement (light blue). Right inset shows correlation of pupil size and ocular movement with HON photometry (n = 7 mice). ***C,*** Partial least squares regression fit to predict HON GCaMP6s photometry from the movement metric, pupil size, and ocular movement. Percent contribution of each feature is quantified using drop-one feature analysis (see methods). ***D,*** Empirical mode decomposition of HON GCaMP6s IMFs to quantify the frequency of HON activity containing the maximum correlation with each feature. Movement metric maximally correlated with HON frequencies that were higher than that of pupil size, but lower than that of ocular movements (Bonferroni-corrected paired *t*-test: against pupil size $t_6 = 3.4199$, * p = 0.0283; against ocular movements $t_6 = 4.6059$, ** p = 0.0073). ***E,*** Local regression displaying coefficient weights from a partial least squares regression fit to individual HON GCaMP6s IMFs, plotted as a function of the IMF's characteristic frequency.

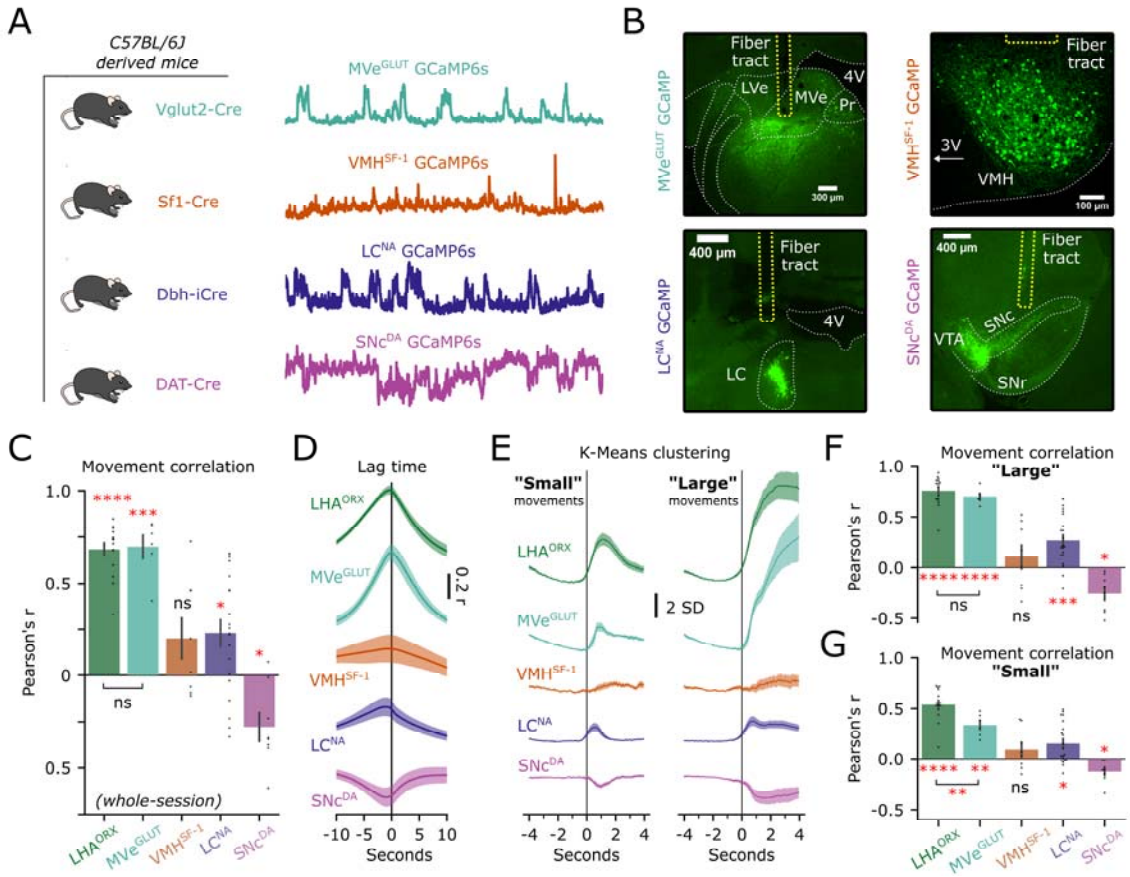

Figure 8. Representation of movement across genetically defined neurons.

A, C57BL/6J-derived strains of mice permitted Cre-dependent photometry recordings from four separate neural populations (MVe^{GLUT}, n = 6; VMH^{SF-1}, n = 8; LC^{NA}, n = 20; and SNc^{DA}, n = 8 mice). ***B,*** Representative histology from each recording site. LVe; lateral vestibular nucleus; MVe; medial vestibular nucleus; Pr; nucleus prepositus; 4V; fourth ventricle; VMH; ventral medial hypothalamus 3V; third ventricle; LC; locus coeruleus; VTA; ventral tegmental area; SNc; substantia nigra pars compacta; SNr; substantia nigra pars reticulata. ***C,*** Whole-session correlation of movement with photometry across neural subtypes. Asterisks represent one sample *t*-tests against mean of zero, after Bonferroni correction. Additional comparison is shown between LHA^{ORX} (HONs, n = 15 mice) and MVe^{GLUT} neurons (unpaired *t*-test: $t_{19} = 0.209$, p = 0.8366). ***D,*** Cross correlation displaying lag time of each recorded population. Negative values imply photometry precedes movement. Lines and shaded regions represent mean ± SEM. ***E,*** Photometry baselined -3 to -1 seconds before movement initiation in two clusters: small movements (left) and large movements (right). Lines and shaded regions represent mean ± SEM. ***F.*** Correlation of movement and photometry during initiation of large movements. Asterisks represent one sample *t*-tests against mean of zero, after Bonferroni correction. Additional comparison is shown between HONs (LHA^{ORX}) and MVe^{GLUT} (unpaired *t*-test: $t_{19} = 0.877$, p = 0.3915). ***G.*** Correlation of movement and photometry during initiation of small movements. Asterisks represent one sample *t*-tests against mean of zero, after Bonferroni correction. Additional comparison is shown between LHA^{ORX} (HONs) and MVe^{GLUT} (unpaired *t*-test: $t_{19} = 2.864$, p = 0.0099).

*p < 0.05, **p < 0.01, ***p < 0.001, ****p < 0.0001 and ns, not significant by two-tailed tests.

References:

1. Stringer, C., *et al.* Spontaneous behaviors drive multidimensional, brainwide activity. *Science* **364**, 255 (2019).
2. Musall, S., Kaufman, M.T., Juavinett, A.L., Gluf, S. & Churchland, A.K. Single-trial neural dynamics are dominated by richly varied movements. *Nat Neurosci* **22**, 1677-1686 (2019).
3. Wang, A.W., *et al.* Not everything, not everywhere, not all at once: a study of brain-wide encoding of movement. *bioRxiv* https://doi.org/10.1101/2023.06.08.544257 (2023).
4. Zagha, E., *et al.* The Importance of Accounting for Movement When Relating Neuronal Activity to Sensory and Cognitive Processes. *J Neurosci* **42**, 1375-1382 (2022).
5. Carpenter, R. & Reddi, B. *Neurophysiology* (CRC Press, 2012).
6. Crochet, S. & Petersen, C.C. Correlating whisker behavior with membrane potential in barrel cortex of awake mice. *Nat Neurosci* **9**, 608-610 (2006).
7. Deschenes, M., Moore, J. & Kleinfeld, D. Sniffing and whisking in rodents. *Curr Opin Neurobiol* **22**, 243-250 (2012).
8. Herrington, T.M., *et al.* The effect of microsaccades on the correlation between neural activity and behavior in middle temporal, ventral intraparietal, and lateral intraparietal areas. *J Neurosci* **29**, 5793-5805 (2009).
9. Keller, G.B., Bonhoeffer, T. & Hubener, M. Sensorimotor mismatch signals in primary visual cortex of the behaving mouse. *Neuron* **74**, 809-815 (2012).
10. Martinez-Conde, S., Macknik, S.L. & Hubel, D.H. Microsaccadic eye movements and firing of single cells in the striate cortex of macaque monkeys. *Nat Neurosci* **3**, 251-258 (2000).
11. Miura, S.K. & Scanziani, M. Distinguishing externally from saccade-induced motion in visual cortex. *Nature* **610**, 135-142 (2022).
12. Niell, C.M. & Stryker, M.P. Modulation of visual responses by behavioral state in mouse visual cortex. *Neuron* **65**, 472-479 (2010).
13. Salkoff, D.B., Zagha, E., McCarthy, E. & McCormick, D.A. Movement and Performance Explain Widespread Cortical Activity in a Visual Detection Task. *Cereb Cortex* **30**, 421-437 (2020).
14. Schneider, D.M. & Mooney, R. Motor-related signals in the auditory system for listening and learning. *Curr Opin Neurobiol* **33**, 78-84 (2015).
15. Vinck, M., Batista-Brito, R., Knoblich, U. & Cardin, J.A. Arousal and locomotion make distinct contributions to cortical activity patterns and visual encoding. *Neuron* **86**, 740-754 (2015).
16. West, S.L., *et al.* Wide-Field Calcium Imaging of Dynamic Cortical Networks during Locomotion. *Cereb Cortex* **32**, 2668-2687 (2022).
17. Yu, J., Gutnisky, D.A., Hires, S.A. & Svoboda, K. Layer 4 fast-spiking interneurons filter thalamocortical signals during active somatosensation. *Nat Neurosci* **19**, 1647-1657 (2016).
18. Bimbard, C., *et al.* Behavioral origin of sound-evoked activity in mouse visual cortex. *Nat Neurosci* **26**, 251-258 (2023).
19. de Lecea, L., *et al.* The hypocretins: hypothalamus-specific peptides with neuroexcitatory activity. *Proc Natl Acad Sci U S A* **95**, 322-327 (1998).
20. Sakurai, T., *et al.* Orexins and orexin receptors: A family of hypothalamic neuropeptides and G protein-coupled receptors that regulate feeding behavior. *Cell* **92**, 573-585 (1998).
21. Yamanaka, A., *et al.* Hypothalamic orexin neurons regulate arousal according to energy balance in mice. *Neuron* **38**, 701-713 (2003).

22. Burdakov, D., Gerasimenko, O. & Verkhratsky, A. Physiological changes in glucose differentially modulate the excitability of hypothalamic melanin-concentrating hormone and orexin neurons in situ. *J Neurosci* **25**, 2429-2433 (2005).
23. Viskaitis, P.*, et al.* Orexin neurons track temporal features of blood glucose in behaving mice. *Nat Neurosci* **27**, 1299-1308 (2024).
24. Chemelli, R.M.*, et al.* Narcolepsy in orexin knockout mice: molecular genetics of sleep regulation. *Cell* **98**, 437-451 (1999).
25. Lin, L.*, et al.* The sleep disorder canine narcolepsy is caused by a mutation in the hypocretin (orexin) receptor 2 gene. *Cell* **98**, 365-376 (1999).
26. Adamantidis, A.R., Zhang, F., Aravanis, A.M., Deisseroth, K. & de Lecea, L. Neural substrates of awakening probed with optogenetic control of hypocretin neurons. *Nature* **450**, 420-424 (2007).
27. Sakurai, T. The role of orexin in motivated behaviours. *Nat Rev Neurosci* **15**, 719-731 (2014).
28. Thannickal, T.C.*, et al.* Reduced number of hypocretin neurons in human narcolepsy. *Neuron* **27**, 469-474 (2000).
29. Peyron, C.*, et al.* Neurons containing hypocretin (orexin) project to multiple neuronal systems. *J Neurosci* **18**, 9996-10015 (1998).
30. Thannickal, T.C., Lai, Y.Y. & Siegel, J.M. Hypocretin (orexin) cell loss in Parkinson's disease. *Brain* **130**, 1586-1595 (2007).
31. Nishino, S., Ripley, B., Overeem, S., Lammers, G.J. & Mignot, E. Hypocretin (orexin) deficiency in human narcolepsy. *Lancet* **355**, 39-40 (2000).
32. Peyron, C.*, et al.* A mutation in a case of early onset narcolepsy and a generalized absence of hypocretin peptides in human narcoleptic brains. *Nat Med* **6**, 991-997 (2000).
33. Johnson, P.L.*, et al.* A key role for orexin in panic anxiety. *Nat Med* **16**, 111-115 (2010).
34. Dauvilliers, Y.*, et al.* Daridorexant, a New Dual Orexin Receptor Antagonist to Treat Insomnia Disorder. *Ann Neurol* **87**, 347-356 (2020).
35. Bassetti, C.L.A.*, et al.* Narcolepsy - clinical spectrum, aetiopathophysiology, diagnosis and treatment. *Nat Rev Neurol* **15**, 519-539 (2019).
36. Nishino, S.*, et al.* Low cerebrospinal fluid hypocretin (Orexin) and altered energy homeostasis in human narcolepsy. *Ann Neurol* **50**, 381-388 (2001).
37. Placais, P.Y. & Preat, T. To favor survival under food shortage, the brain disables costly memory. *Science* **339**, 440-442 (2013).
38. Chen, T.-W.*, et al.* Ultrasensitive fluorescent proteins for imaging neuronal activity. in *Nature* 295-300 (Nature Research, 2013).
39. Huang, N.E.*, et al.* The empirical mode decomposition and the Hilbert spectrum for nonlinear and non-stationary time series analysis. *Proceedings of the Royal Society A* **454**, 903-995 (1998).
40. Gonzalez, J.A.*, et al.* Inhibitory Interplay between Orexin Neurons and Eating. *Current Biology* **26**, 2486-2491 (2016).
41. Viskaitis, P.*, et al.* Ingested non-essential amino acids recruit brain orexin cells to suppress eating in mice. *Curr Biol* **32**, 1812-1821 e1814 (2022).
42. Aston-Jones, G. & Waterhouse, B. Locus coeruleus: From global projection system to adaptive regulation of behavior. *Brain Res* **1645**, 75-78 (2016).
43. Bear, M.F., Connors, B.W. & Paradiso, M.A. *Neuroscience: Exploring the Brain* (Jones & Barlett Pub Inc, USA, 2015).
44. Marcus, J.N.*, et al.* Differential expression of orexin receptors 1 and 2 in the rat brain. *The Journal of comparative neurology* **435**, 6-25 (2001).

45. Duffet, L., *et al.* A genetically encoded sensor for in vivo imaging of orexin neuropeptides. *Nat Methods* **19**, 231-241 (2022).
46. Cai, X.J., *et al.* Hypothalamic orexin expression: modulation by blood glucose and feeding. *Diabetes* **48**, 2132-2137 (1999).
47. Mileykovskiy, B.Y., Kiyashchenko, L.I. & Siegel, J.M. Behavioral correlates of activity in identified hypocretin/orexin neurons. *Neuron* **46**, 787-798 (2005).
48. Lee, M.G., Hassani, O.K. & Jones, B.E. Discharge of identified orexin/hypocretin neurons across the sleep-waking cycle. *J Neurosci* **25**, 6716-6720 (2005).
49. Bradley, M.M., Miccoli, L., Escrig, M.A. & Lang, P.J. The pupil as a measure of emotional arousal and autonomic activation. *Psychophysiology* **45**, 602-607 (2008).
50. Grujic, N., Polania, R. & Burdakov, D. Neurobehavioral meaning of pupil size. *Neuron* (2024).
51. Grujic, N., Tesmer, A., Bracey, E., Peleg-Raibstein, D. & Burdakov, D. Control and coding of pupil size by hypothalamic orexin neurons. *Nat Neurosci* **26**, 1160-1164 (2023).
52. Horowitz, S.S., Blanchard, J. & Morin, L.P. Medial vestibular connections with the hypocretin (orexin) system. *J Comp Neurol* **487**, 127-146 (2005).
53. Carter, M.E., *et al.* Tuning arousal with optogenetic modulation of locus coeruleus neurons. *Nat Neurosci* **13**, 1526-1533 (2010).
54. Korotkova, T.M., Sergeeva, O.A., Eriksson, K.S., Haas, H.L. & Brown, R.E. Excitation of ventral tegmental area dopaminergic and nondopaminergic neurons by orexins/hypocretins. *J Neurosci* **23**, 7-11 (2003).
55. da Silva, J.A., Tecuapetla, F., Paixão, V. & Costa, R.M. Dopamine neuron activity before action initiation gates and invigorates future movements. in *Nature* 244-248 (Nature Publishing Group, 2018).
56. Hagan, J.J., *et al.* Orexin A activates locus coeruleus cell firing and increases arousal in the rat. *Proc Natl Acad Sci U S A* **96**, 10911-10916 (1999).
57. Horvath, T.L., *et al.* Hypocretin (orexin) activation and synaptic innervation of the locus coeruleus noradrenergic system. *The Journal of comparative neurology* **415**, 145-159 (1999).
58. Choi, Y.H., Fujikawa, T., Lee, J., Reuter, A. & Kim, K.W. Revisiting the Ventral Medial Nucleus of the Hypothalamus: The Roles of SF-1 Neurons in Energy Homeostasis. *Front Neurosci* **7**, 71 (2013).
59. Viskaitis, P., *et al.* Modulation of SF1 Neuron Activity Coordinately Regulates Both Feeding Behavior and Associated Emotional States. in *Cell reports* 3559-3572 (Elsevier, 2017).
60. Tong, Q., *et al.* Synaptic glutamate release by ventromedial hypothalamic neurons is part of the neurocircuitry that prevents hypoglycemia. in *Cell Metabolism* 383-393 (2007).
61. Meek, T.H., *et al.* Functional identification of a neurocircuit regulating blood glucose. *Proc Natl Acad Sci U S A* **113**, E2073-2082 (2016).
62. Deem, J.D., *et al.* Identification of Hypothalamic Glucoregulatory Neurons That Sense and Respond to Changes in Glycemia. *Diabetes* **72**, 1207-1213 (2023).
63. Chen, C.T., Hwang, L.L., Chang, J.K. & Dun, N.J. Pressor effects of orexins injected intracisternally and to rostral ventrolateral medulla of anesthetized rats. *Am J Physiol Regul Integr Comp Physiol* **278**, R692-697 (2000).
64. Shahid, I.Z., Rahman, A.A. & Pilowsky, P.M. Orexin and central regulation of cardiorespiratory system. *Vitamins and hormones* **89**, 159-184 (2012).
65. Williams, R.H. & Burdakov, D. Hypothalamic orexins/hypocretins as regulators of breathing. *Expert Rev Mol Med* **10**, e28 (2008).

66. Kuwaki, T. Orexinergic modulation of breathing across vigilance states. *Respir Physiol Neurobiol* (2008).
67. Karnani, M. & Burdakov, D. Multiple hypothalamic circuits sense and regulate glucose levels. in *American journal of physiology. Regulatory, integrative and comparative physiology* R47-55 (American Physiological Society, 2011).
68. DiStefano, J., Stubberud, A. & Williams, I. *Feedback and Control Systems* (McGrawHill, 2012).
69. Aström, K. & Hagglund, T. *PID controllers: Theory, Design, and Tuning* (Intrument Society of America, 1995).
70. Crapse, T.B. & Sommer, M.A. Corollary discharge across the animal kingdom. *Nat Rev Neurosci* **9**, 587-600 (2008).
71. Karnani, M.M.*, et al.* Role of spontaneous and sensory orexin network dynamics in rapid locomotion initiation. *Prog Neurobiol* **187**, 101771 (2020).
72. Donegan, D., Peleg-Raibstein, D., Lambercy, O. & Burdakov, D. Anticipatory countering of motor challenges by premovement activation of orexin neurons. *PNAS Nexus* **1** (2022).
73. Donegan, D.*, et al.* Hypothalamic Control of Forelimb Motor Adaptation. *J Neurosci* **42**, 6243-6257 (2022).
74. Giardino, W.J.*, et al.* Parallel circuits from the bed nuclei of stria terminalis to the lateral hypothalamus drive opposing emotional states. *Nat Neurosci* **21**, 1084-1095 (2018).
75. Samson, W.K., Bagley, S.L., Ferguson, A.V. & White, M.M. Orexin receptor subtype activation and locomotor behaviour in the rat. *Acta Physiol (Oxf)* **198**, 313-324 (2010).
76. Li, H.T., Viskaitis, P., Bracey, E., Peleg-Raibstein, D. & Burdakov, D. Transient targeting of hypothalamic orexin neurons alleviates seizures in a mouse model of epilepsy. *Nat Commun* **15**, 1249 (2024).
77. Li, H.T., Donegan, D.C., Peleg-Raibstein, D. & Burdakov, D. Hypothalamic deep brain stimulation as a strategy to manage anxiety disorders. *Proc Natl Acad Sci U S A* **119**, e2113518119 (2022).
78. Hara, J.*, et al.* Genetic ablation of orexin neurons in mice results in narcolepsy, hypophagia, and obesity. *Neuron* **30**, 345-354 (2001).
79. Ripley, B.*, et al.* CSF hypocretin/orexin levels in narcolepsy and other neurological conditions. *Neurology* **57**, 2253-2258 (2001).
80. International Brain, L.*, et al.* Standardized and reproducible measurement of decision-making in mice. *Elife* **10** (2021).
81. Guo, Z.V.*, et al.* Procedures for behavioral experiments in head-fixed mice. *PLoS One* **9**, e88678 (2014).
82. Shimaoka, D., Harris, K.D. & Carandini, M. Effects of Arousal on Mouse Sensory Cortex Depend on Modality. *Cell Rep* **22**, 3160-3167 (2018).
83. Lu, L.*, et al.* Control of locomotor speed, arousal, and hippocampal theta rhythms by the nucleus incertus. *Nat Commun* **11**, 262 (2020).
84. Breton-Provencher, V. & Sur, M. Active control of arousal by a locus coeruleus GABAergic circuit. *Nat Neurosci* **22**, 218-228 (2019).
85. Hulsey, D., Zumwalt, K., Mazzucato, L., McCormick, D.A. & Jaramillo, S. Decision-making dynamics are predicted by arousal and uninstructed movements. *Cell Rep* **43**, 113709 (2024).
86. Zahler, S.H., Taylor, D.E., Wong, J.Y., Adams, J.M. & Feinberg, E.H. Superior colliculus drives stimulus-evoked directionally biased saccades and attempted head movements in head-fixed mice. *Elife* **10** (2021).

87. Gonzalez, J.A., Iordanidou, P., Strom, M., Adamantidis, A. & Burdakov, D. Awake dynamics and brain-wide direct inputs of hypothalamic MCH and orexin networks. *Nat Commun* **7**, 11395 (2016).
88. Schöne, C., Apergis-Schoute, J., Sakurai, T., Adamantidis, A. & Burdakov, D. Coreleased orexin and glutamate evoke nonredundant spike outputs and computations in histamine neurons. *Cell Rep* **7**, 697-704 (2014).
89. Baimel, C., Lau, B.K., Qiao, M. & Borgland, S.L. Projection-Target-Defined Effects of Orexin and Dynorphin on VTA Dopamine Neurons. *Cell Rep* **18**, 1346-1355 (2017).
90. Crocker, A.*, et al.* Concomitant loss of dynorphin, NARP, and orexin in narcolepsy. *Neurology* **65**, 1184-1188 (2005).
91. Parlato, R., Otto, C., Begus, Y., Stotz, S. & Schutz, G. Specific ablation of the transcription factor CREB in sympathetic neurons surprisingly protects against developmentally regulated apoptosis. *Development* **134**, 1663-1670 (2007).
92. Mathis, A.*, et al.* DeepLabCut: markerless pose estimation of user-defined body parts with deep learning. *Nat Neurosci* **21**, 1281-1289 (2018).
93. Nath, T.*, et al*. Using DeepLabCut for 3D markerless pose estimation across species and behaviors. in *Nature Protocols* 2152-2176 (Nature Publishing Group, 2019).
94. He, K., Zhang, X., Ren, S. & Sun, J. Deep Residual Learning for Image Recognition. *arXiv:1512.03385* (2015).
95. Crombie, D., Spacek, M.A., Leibold, C. & Busse, L. Spiking activity in the visual thalamus is coupled to pupil dynamics across temporal scales. *PLoS Biol* **22**, e3002614 (2024).
96. Quinn, A.J., Lopes-Dos-Santos, V., Dupret, D., Nobre, A.C. & Woolrich, M.W. EMD: Empirical Mode Decomposition and Hilbert-Huang Spectral Analyses in Python. *J Open Source Softw* **6** (2021).
97. Engelhard, B.*, et al.* Specialized coding of sensory, motor and cognitive variables in VTA dopamine neurons. *Nature* **570**, 509-513 (2019).